PCCP

PAPER

View Article Online
View Journal | View Issue

Cite this: *Phys. Chem. Chem. Phys.*, 2025, **27**, 21739

Insights into the oxygen evolution mechanism of transition metal-anchored holey graphyne

K. Simmy Joseph, [a] Brahmananda Chakraborty *[bc] and Shweta Dabhi *[a]

Received 3rd June 2025,
Accepted 11th September 2025

DOI: 10.1039/d5cp02097b

rsc.li/pccp

Growing worldwide environmental concerns linked to the overuse of fossil fuels and rising energy demands are driving a thorough and comprehensive search for clean, sustainable sources of energy. Water electrolysis has recently become a highly appealing method for achieving optimal energy conversion and storage. This study employs density functional theory to investigate the catalytic performance along with the electronic properties of pristine and adatom-doped transition metal (TMs = Sc, Pt, Co, Cr, and Au)-anchored holey graphyne (HGY). Among all considered candidates, Pt-doped HGY gives the best oxygen evolution reaction (OER) with the overpotential equivalent to 0.74 V. This catalyst is deemed optimal for further exploration of the OER mechanism. Through molecular dynamics (MD) simulations, the structural along with thermal stability of Pt@HGY has been confirmed. The convincing results motivate the use of Pt-anchored HGY as an efficient OER mechanism catalyst.

Introduction

The pressing issue of meeting the increasing energy demand caused by rising populations and societal progress must be addressed without delay. The oxygen evolution reaction is hindered by its slow kinetics, which is caused by a complex multielectron reaction process. As a result, the reaction requires a greater overpotential in order to provide a sufficient current for the OER. Noble metal-based compounds such as IrO_2 and RuO_2 are commonly used as commercial electrocatalysts for the OER.[1–3] The limited availability and expensive cost severely restrict their use on a large commercial level. Significant efforts have been made in this case to determine which earth-copious components are suitable for OER catalysis.[4,5] The rate-determining step (RDS), which is the adsorption as well as the desorption of intermediates onto the active site, determines the kinetics of the OER; the effectiveness of this step is correlated with the active site's d-orbital electronic structure. Consequently, adjusting the electronic structure of the electrochemical reaction's active site at the atomic scale is a useful way to enhance the electrochemical performance of electrode materials. The elementary phase of oxygen evolution, which involves the formation of an O–O bond and the complex transfer of 4 protons along with 4 electrons, is considered to be the slowest despite having the highest activation energy.[6–8] As a result, the reaction exhibits a relatively low level of efficiency, hence impeding its practical application. Nevertheless, due to the sluggish four-electron transfer, catalysts are indispensable for the vast majority of OER processes, and the prohibitively high cost of existing noble metal-based catalysts is a critical weakness to sustainable chemistry as well as industrialization.[9,10] Efficient electrocatalysts are necessary to control the overpotential and accelerate the process. Throughout the literature, it has been recognised that oxides of iridium and ruthenium are the most suitable options for catalysing the process of oxygen evolution,[11–16] as they are cost-efficient yet exhibit comparable performance. Hence, it is essential for researchers to possess a thorough comprehension of the reaction mechanisms implicated in every phase of the OER and strategically devise catalysts that can adequately meet market requirements, including water splitting reaction devices and metal air batteries. The OER is a vital reaction that plays a key part in a number of renewable energy technologies, such as metal air batteries and water splitting.[17–20]

Two-dimensional (2D) materials possess intriguing characteristics, including a substantial surface area, excellent thermal as well as mechanical stability, and adjustable electronic properties, along with versatility in various research domains and applications such as gas sensors, spintronics, energy storage, *etc.*[16,21,22] These attributes have contributed to their increasing popularity in recent times. Examples of these materials include porous carbon compounds like graphene, and transition metal dichalcogenides (TMDCs) such as MoS_2, WS_2, and VSe_2, and hexagonal boron nitride, to name a few.[14,15,17,20] Because of the previously described qualities, high sensitivity, selectivity, and

[a] *Department of Physical Science, P. D. Patel Institute of Applied Sciences, Charotar University of Science and Technology, CHARUSAT Campus, Changa, 388421, Gujarat, India. E-mail: shwetadabhi.phys@charusat.ac.in*
[b] *High Pressure and Synchrotron Radiation Physics Division, Bhabha Atomic Research Centre, Mumbai, India. E-mail: brahma@barc.gov.in*
[c] *Homi Bhabha National Institute, Mumbai, 400085, India*

quick recovery, 2D materials are now widely used as efficient catalysts to develop electrocatalytic processes.[23] Graphene is an exceptionally desirable nanomaterial on account of its remarkable mechanical strength, and phononic and captivating electro-optical characteristics, as it is composed of carbon atoms arranged in the most stable 2D configuration. The characteristics exhibited by graphene have resulted in significant progress within the domains of contemporary chemistry and physics. The electrical structure of graphene, characterised by a zero-bandgap, imposes limitations on its use within the domain of semiconducting materials. Thereupon, it is crucial to identify avant-garde types of two-dimensional carbon allotropes that demonstrate peculiar semiconducting properties, for instance an appropriate energy bandgap and enhanced mobility.[24–27] Graphene possesses a honeycomb lattice structure, while graphyne exhibits several geometrical configurations. At present, scholars have predominantly examined four unique geometries of graphynes, *viz.* a-, b-, g-, and 6,6,12-graphyne.[28–30] The remarkable attributes of graphyne make them strong competitors to graphene, especially in specific applications. The design and coalescence of the anecdote carbon allotrope, namely holey graphyne (HGY), was inspired by this intriguing molecule, as reported. The atomic structure of HGY is characterised by the presence of uniform pores arranged in 6, 8, and 24 vertex rings. The rings are surrounded by acetylene connections of zero, two, and six, which are produced through sp–sp bonds. Two C atoms from the benzene ring are joined to 2 C atoms from the following octagon to provide a 50% sp to sp^2 C ratio.[31] It was previously found that HGY is composed of a p-type semiconductor that has elevated electron and Hall mobilities. At ambient temperature, the system exhibits a hole mobility of 2.13×10^9 cm^2 V^{-1} s^{-1}, an electron mobility of about 10^4 cm^2 V^{-1} s^{-1}, and a band gap of 1.0 eV.[32] Then, in 2021, Gao *et al.* determined that the overall gravimetric density of Li-coated HGY could surge to 12.8% when they investigated its H_2 storage capacity.[33] An investigation conducted in 2022 by Xinghui *et al.* examined the stability, vibrational, and optical properties of HGY. The researchers discovered that HGY sheets synthesized with AB stacking are exceptionally crystalline. The semiconducting nature, nonlinear sp bonding, and unique pi-conjugated structure of HGY make it very suitable for a wide range of applications.[34] In their research, Juhee *et al.* investigated the adsorption and desorption properties of hydrogen (H) in the Ti-functionalized HGY system. It was also observed that the titanium atom exhibits an adsorption energy of −0.38 electron Volt per hydrogen atom, which allows it to gather seven H_2 molecules. The outcome of this process yields a hydrogen gravimetric density of 10.52 weight percent.[35] Subsequently, the H storage potential of HGY anchored with Sc as well as Y was examined by Mukesh *et al.* They discovered that the gravimetric densities could reach 9.80% and 9.34%.[36] In a study conducted in 2023, Seetha *et al.* examined the detection of ammonia on HGY, decorated with Cu, Sc, and Pd. The results showed that among all the decorations, Sc-doped HGY was identified as the best NH_3 sensor. At a temperature of 600 K, the sample demonstrated an adsorption energy of 1.49 eV, a notable charge transfer of 0.113*e*, and a recoverable time of 3.2 s.[37] Darshil *et al.* conducted a study which showed that the HGY catalysts, doped with different TMs like Fe, Cr, and Co, exhibit a high level of activity for the HER with ΔG values as low as −0.21, −0.14, and −0.05 electron Volt.[31] Manman *et al.* found that SACs buoyed by graphydiyne and holey graphyne are a potential option for the CO_2RR after studying them using machine learning. By considering the complete elemental miscellany of metal sites across the periodic table, it was discovered that 25 catalysts could both successfully activate CO_2 along with the HER.[38] Muhammad *et al.* examined the potential of HGY for battery applications, and it was observed that compared to other carbonaceous materials (200–500 mAh g^{-1} for Na and 450–750 mAh g^{-1} for Li) and traditional graphite anodes (372 mAh g^{-1} for Li and <35 mAh g^{-1} for Na), Na (558 mAh g^{-1}) was revealed to have much larger storage capacities.[39] Bohayra examined the mechanical, electrical, and thermal characteristics of C and BN-HGY and discovered that the semiconducting C-HGY along with insulating NB-HGY system had moderate lattice thermal conductivity and ultrahigh negative thermal expansion coefficients.[40] Yong *et al.* have examined a higher-order topological invariant connected to the material's C2 symmetry and proved that the ensuing corner modes materialize in nanoflakes that match the hitherto disclosed precursor structure.[41] While initial theoretical reckoning of HGY have been documented for applications such as hydrogen storage, battery technology, and catechol detection; HGY's potential as a general water splitting mechanism involving certain transition metals with the OER remains unexplored.

In this study, we report using DFT simulations, an unprecedentedly potent way of oxygen evolution *via* pristine and transition metal (TM = Au, Co, Cr, Pt, and Sc) HGY monolayers. The utilisation of theoretical simulations aids in the clarification of the adsorption mechanism at the orbital level. These insights include favourable adsorption configurations, adsorption energy, bonding angle and distance, charge transfer, and binding energy. In light of theoretical considerations such as adsorption energy, Löwdin charge analysis and partial density of states, the phenomenon of charge transfer has been examined. Additionally, it has been observed that even at extremely high temperatures up to 500 K, the Pt element maintains its binding with HGY. These *ab initio* molecular dynamics simulations provide additional substantiation for the thermal stability of the system.

Computational methodology

Quantum ESPRESSO was used to perform calculations in accordance with density functional theory (DFT).[42,43] The generalized gradient approximation (GGA) was used to represent the exchange–correlation energies, and the projector augmented wave (PAW) potentials were used to analyse the electron–ion interactions.[44] Integration over the Brillouin zone was conducted utilising a *k*-point mesh of $5 \times 5 \times 1$ and a plane wave

kinetic energy cutoff of 50 Ry. Both the atomic positions and the structural parameters were relaxed until the energy reached a convergence of 10^{-6} eV, respectively. A 20 Å vacuum was used to eliminate the imperceptible forces betwixt neighbouring layers in the *z*-direction. The utilisation of Grimme's DFT-D2 strategies was implemented in order to tackle the extended van der Waals interactions that encompass heterostructures and bilayers.[45] The thermal and structural stability have been verified by molecular dynamics simulations, utilizing the VASP[46] code.

Results and discussion

Structural, binding energy and electronic properties, and the OER mechanism of pristine HGY and TM-anchored HGY

The lattice constants for pristine HGY were determined to be 10.796 Å based on the hexagonal unit cell's structure. Fig. 1(a and b) show the 24 C atoms that make up the HGY supercell. By applying an adamant vacuum level of 20 Å across the aperiodic orientation and fully relaxing the atomic position with regard to cell size, the pristine HGY supercells were optimized.

The scrutiny of pristine HGY and its function in the OER process of water splitting will be covered. O adsorption alone is not a reliable signal for forecasting OER reactions, according to a literature review. The entire activity of the OER, comprising OH, O, and OOH intermediates, has been distinctly surveyed in this research work. The adsorption geometries of HGY with the potential adsorption sites are shown in Fig. 1(c).

Fig. 1 shows the optimised geometry of the HGY monolayer from both (a) top view and (b) side perspectives. The optimal bond lengths (Å) along with the bond angles (°) of OER intermediates (O, OH, and OOH) adsorbed at various potential adsorption sites (P1–P9) on pristine HGY are summarized in Table S1. The lengths of the C–C bonds proximal to the binding site for O adsorption range from 1.21 to 1.32 Å, whereas those next to the binding site extend slightly up to 1.47 Å. The site-dependent lattice distortions caused by O anchoring are indicated by the large fluctuation in the C–C–O bond angles, which range from 61.9° at P4 to as high as 143.3° at P2 and P5. In accordance with molecular stability, the O–O (≈1.36–1.38 Å) and O–H (≈0.98 Å) bond lengths in the event of OOH adsorption stay almost constant across all locations. Disparities in adsorption strength and contact distance with the HGY surface are reflected in the O–C bond lengths, which range greatly from 2.47 Å (P1) to 3.10 Å (P9). The angular parameters likewise exhibit a substantial dependency on the adsorption site: the O–O–H angle is typically about 103°, the C–C–O angle ranges from 83.5° (P4) to 114.3° (P7), and the C–O–O angle ranges from 107.6° (P1) to 173.2° (P7). According to these findings, the inherent OOH geometry is maintained, although the binding orientation and HGY interaction differ considerably depending on the adsorption location.

Overall, the structural study shows that O adsorption results in localized bond distortions, while OOH adsorption, particularly at sites P7 and P9, produces greater fluctuations in adsorption distance along with angular distortion. The sensitivity of pristine HGY to intermediate binding is highlighted by its site-specific structural flexibility, which is essential for comprehending its catalytic action in the OER. Although stronger binding sites like P1 and P2 run the risk of over binding and impairing the reaction kinetics, they may effectively stabilize intermediates. On the other hand, OOH, the crucial intermediate in the OER, is frequently destabilized by weaker binding sites like P7 and P9, which lessens its catalytic significance.

In order to provide a detailed elucidation of the adsorption reaction mechanism, the HGY transition state was calculated. Initially, the reaction included a proton being transferred to an adsorbed OH molecule *via* a surface-adsorbed H_2O molecule. A proton is released by the adsorbed hydroxide (OH), creating an adsorbed atomic oxygen. Adsorbed hydroperoxyl (OOH) is the result of this atomic oxygen's subsequent reaction with OH^-

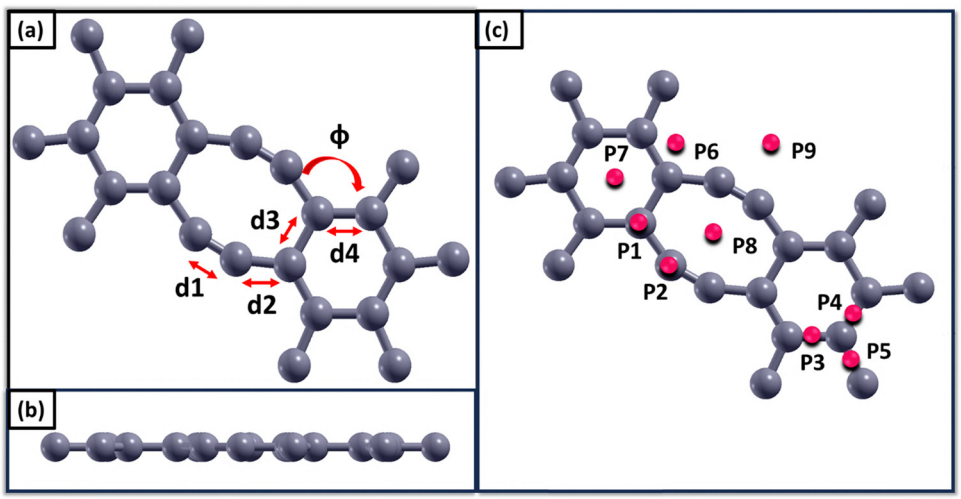

Fig. 1 (a) Top and (b) side view of HGY, and (c) pictorial depiction of HGY for OER activity with possible adsorption sites represented by pink circles. Colour scheme: silver C; pink OER activity.

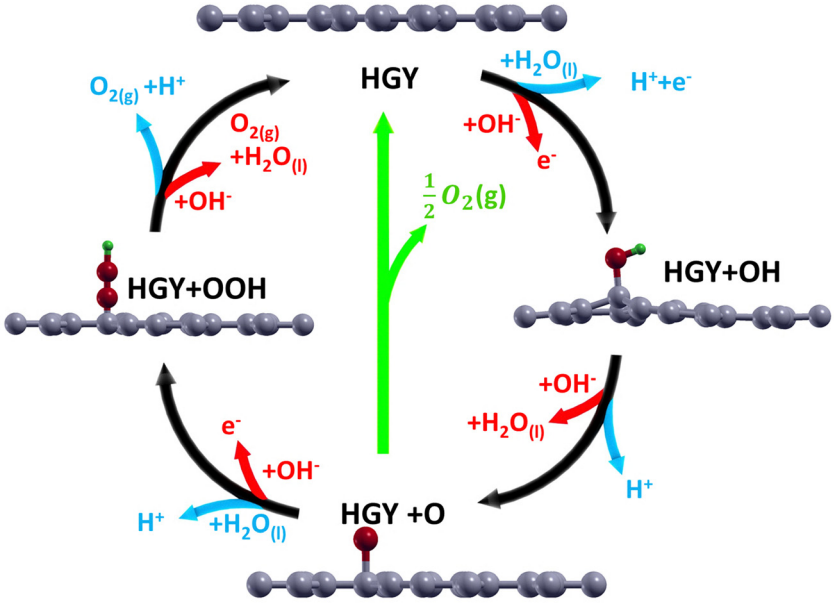

Fig. 2 Schematic representation of the typical OER pathway for pristine HGY. Colour scheme: silver C; red O; green H.

(hydroxide). The adsorbed OOH and its original surface were transformed into molecular O_2 in the fourth step. Fig. 2 illustrates the adsorption of OH on the slab and the genesis of *OOH by the adsorption of *O on OH, releasing energy in accordance with chemical principles. According to the Gibbs free energy diagram, spontaneity was not seen, however, since an external electric field was necessary to perturb the initial electric field balance and promote the movement of the adsorption group. The anaerobic HGY adsorbs species including *O and *OH, as well as *OOH, as depicted in Fig. 2. To ascertain the adsorption energies of the species *OH, *O, and *OOH, we individually attach each species to a different site, such as the top, hollow, and bridge of the carbon atom. Subsequently, we relax the geometry of the system, as illustrated in Fig. 1(c). The hollow sites are denoted by P6, P7, P8, and P9, while P3, P4, and P5 represent the bridge sites between the two carbon atoms, and P1 and P2 represent the C top sites.

The OER is accomplished using procedures (5) to (9) from the SI. The free energy of the reaction was calculated for each individual step.

$$\Delta G = \Delta E + \Delta E_{ZPE} - T\Delta S + \Delta G_U + \Delta G_{pH} \quad (1)$$

The symbol ΔE signifies the total energy change between the initial reactants and final products in a chemical process. The zero-point energy corrections are denoted by ΔZPE. ΔS denotes the alteration in vibrational entropy with respect to a particular temperature T. ΔG_U is equivalent to $-eU$, where U denotes the electrode potential and e^- signifies the fundamental charge. The correction for H^+ free energy is expressed as ΔG_{pH}.[10]

The overpotential, symbolised as η, is calculated by comparing the Gibbs free energy differences at each stage.

$$\eta_{OER} = \max\{\Delta G_1, \Delta G_2, \Delta G_3, \Delta G_4\}/e - 1.23 \quad (2)$$

where ΔG_n are the free energy of reactions (5)–(8) (from the SI).[47,48]

Fig. 3 illustrates the computed reaction energies associated with each OER process taking place at the active sites, as well as the excess potential of pristine HGY. For the purpose of assessment, the utmost reaction energies for the HGY sites were computed as follows: 3.09, 4.12, 2.64, 3.14, 4.12, 3.22, 3.80, 4.03, and 3.93 eV for P1, P2, P3, P4, P5, P6, P8, and P9 (step 3 from OH* to OOH*), and P7 (step 1 from * to OH*). The overpotential values for P1 to P9 are 1.86, 2.89, 1.41, 1.91, 2.89, 1.99, 2.57, 2.80, and 2.70 V, respectively. Following this, the OER activity declines in the subsequent order: P2 > P5 > P8 > P9 > P7 > P6 > P4 > P1 > P3. Inferring from the data from Fig. 3, the activity of the P3 site (bridge site 1) for the OER surpasses those of the other sites of HGY.

The octagon void shown in Fig. 4(a) has been used to anchor the TMs (Au, Pt, Co, Cr, and Sc). The prediction of a structural modification in the HGY is evident from Table S2, which indicates that the interaction between the HGY support and TMs induces a modification in the HGY upon their introduction. The average distances between transition metals (Pt, Sc, Au, Cr, and Co) and the carbon atoms of the HGY support are 2.07, 2.77, 3.06, 2.07, and 1.97 Å, for transition metals attached to HGY.

According to the following relationship, the binding energy is a crucial factor in the recurrent usage of single atom catalysts (SACs):

$$E_b = E(\text{TMs/HGY}) - E(\text{HGY}) - E(\text{TM}) \quad (3)$$

The aggregate energy of the HGY system doped by TMs is designated as E(TMs/HGY), the isolated TM atom's total energy is epitomized by E(TM). The E_b values of the TMs (Au, Co, Cr, Pt, and Sc) on HGY were determined in the current work to be

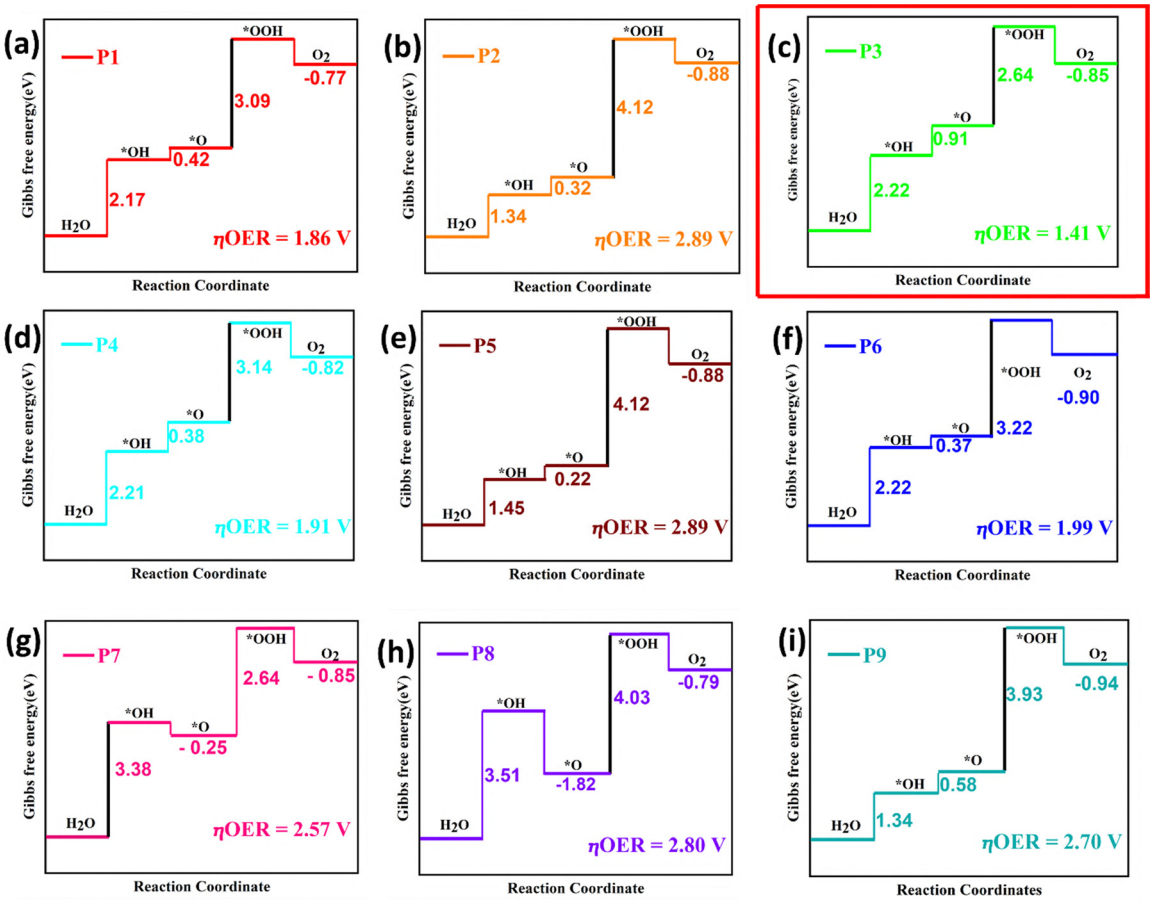

Fig. 3 Free energy diagram of the OER for pristine HGY for all possible sites at zero potential. The black line is the rate determining step of OER activity. (a)–(i) represents sites P1–P9.

−1.40, −2.44, −5.69, −2.45, and −3.60 eV, respectively, using eqn 3. HGY doped with a distinct TM support exhibits a negative magnitude of E_b, which implies a firm binding combined with suitable appropriateness for the substrate of the catalyst (refer to Fig. 4(b)). For instance, Darshil *et al.* found that Zr, Y, V, Sc, Mn, Co, and Fe had binding energies of −4.72, −3.57, −5.23, −2.50, −2.44, −2.27, and −5.69 eV on HGY, respectively.[31] Likewise, the binding energies of −4.09 and −0.69 eV for Sc- and Pd-doped HGY were reported by Seetha *et al.*[49] In comparison, our calculated binding energy for Sc is −4.05 eV, which falls well within the range of previously reported values. A direct comparison, particularly for Sc and other metals, indicates that the slight variations observed among the studies mainly results from differences in pseudopotentials and basis sets used in computational packages such as QE and VASP. Overall, our findings confirm consistency and reliability, as the obtained binding energies align with established literature values.

Simulations were performed by keeping oxygen atom at 2 Å atop the TMs, to investigate the OER process of adatom doping of TMs on HGY. Next, as shown in Fig. 4(c–f [top view] and g–j [side view]), we proceeded to analyse the intermediates of the OER activity, O, OH, and OOH. The adsorption of intermediates causes a modest or minimal change in structural characteristics like bond length and angle in HGY, SACs anchored by TMs. Table S2 makes it evident that this is because of the liaison that takes place between TMs and intermediates. To facilitate comparison, Tables S1 and S2 detail alterations in structural parameters, such as bond length and bond angle, between the HGY-anchored intermediate and TMs HGY SACs. The distance between intermediates such as C–O, O–H, and O–O is between 0.97 and 3.10 Å. The bond lengths spanning from 0.96 to 1.99 Å exist between intermediates such as TM–O, O–H, and O–O, as well as O–H.

In the context of the OER, 4.92 eV is the total energy required to break down water. For the reaction to continue efficiently, the ΔG for each elementary stage in the OER should ideally be minimized. Specifically, the overpotential of the OER must be at least 1.23 eV. Hence, foremost efficient OER catalysts' intermediate Gibbs free energy values will position the total reaction energy around or beneath this threshold. Gibbs free energy profiles and over potential are shown in Fig. 6(a–e) to illustrate the OER process that occurs at the loftiest TMs, comprising Au, Co, Cr, Pt, and Sc, throughout the reaction route.

The maximum reaction energies for the HGY system are found to be as follows: 2.40 eV for Au@HGY (step 2 involves the transformation from OH* to O*), 2.54 eV for Co@HGY [(*OOH to O_2) in step 4], 3.19 eV for Cr@HGY [(*O to *OOH) in step 3],

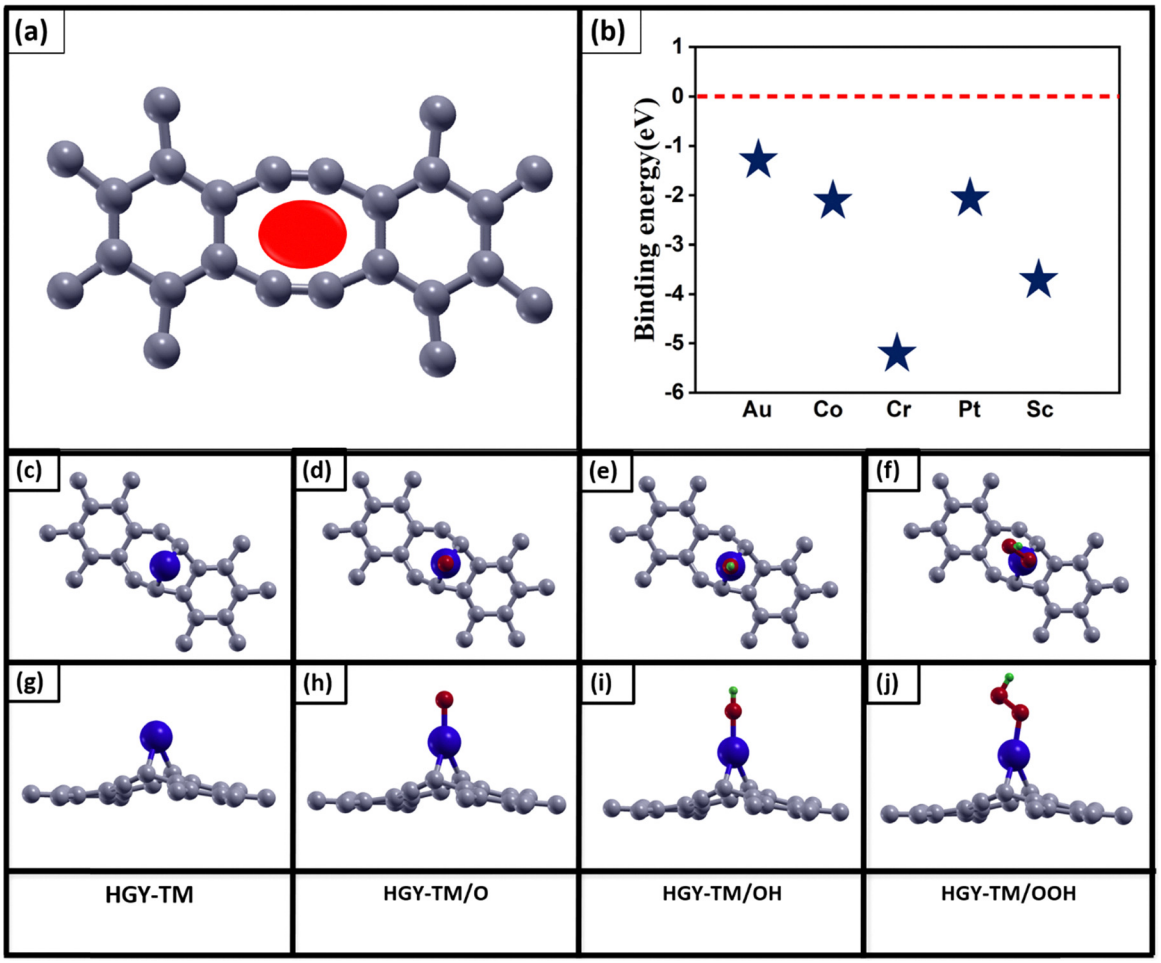

Fig. 4 (a) Energetic position for TM-anchored HGY and (b) binding energy of TM (Au, Co, Cr, Pt, and Sc)-anchored HGY. Top view of (c) TM-HGY (TM = Pt, Au, Co, Cr, and Sc), (d) TM-HGY/O, (e) TM-HGY/OH, and (f) TM-HGY/OOH and side view of (g) TM-HGY (TM = Pt, Au, Co, Cr, and Sc), (h) TM-HGY/O, (i) TM-HGY/OH, and (j) TM-HGY/OOH. Colour scheme: silver C; blue S; navy blue TM; red O; green H.

1.97 eV for Pt@HGY [(*O to *OOH) in step 3], and 3.32 eV for Sc@HGY [(*OOH to O_2) in step 4]. It is found that the maximum reaction energy for Pt@HGY is 1.97 eV, which is significantly closer to the ideal value of 1.23 eV. To boost the OER process, Pt@HGY helps to strengthen the link that forms between the catalyst's surface and the *O intermediate.

The d-band centre is widely recognized as a valuable descriptor for quantifying the strength of the interaction amid adsorbates and catalysts on various surfaces. The following equation is used to determine the d-band centre:

$$\varepsilon_d = \frac{\int_{-\alpha}^{\alpha} p(\varepsilon)\varepsilon d\varepsilon}{\int_{-\alpha}^{\alpha} p(\varepsilon) d\varepsilon} \quad (4)$$

The energy width of the d orbital is represented by ε, while the density of states is represented by ρ.[50] The d orbital of the metal atom has a major impact on the surface electronic structure of transition metals. The projected density of states (PDOS) along with the d band centre ε_d of OH, O, and OOH adsorption on Pt@HGY were investigated in order to better understand the binding properties of the species involved in the associative mechanism (Fig. 7(a–c)). After the intermediates are adsorbed, the d-band centre of each model shows a direction irreconcilable to the Fermi level, with values ranging from −1.15 eV. The metal forfeits excess electrons in order to form an equitable bond with the intermediate due to electron exchange hybridization between the d orbits of Pt@HGY and the sp orbits of the intermediate; additionally, a larger and less appropriate d band centre indicates an enhanced occupancy of antibonding orbitals after the d band of the metal catalyst hybridizes with the s/p band of the adsorbate, leading to the dissociation barrier of the reactants along with enabling the desorption of intermediates across the catalytic reaction system. Moreover, the d band centre boosts by 4.14 electron Volt due to the connection that links H and *OH creating *O. This result supports the theory that electrons can occupy the antibonding orbitals when the H atom is present. Likewise, when the *O is bonded with the –OH, it experiences greater electron loss due to orbital hybridization; as a result, the *OOH exhibits a greater density of states in proximity to the Fermi level, which further reduces the d band centre. According to these findings, the electronic field as well as metal properties have a direct

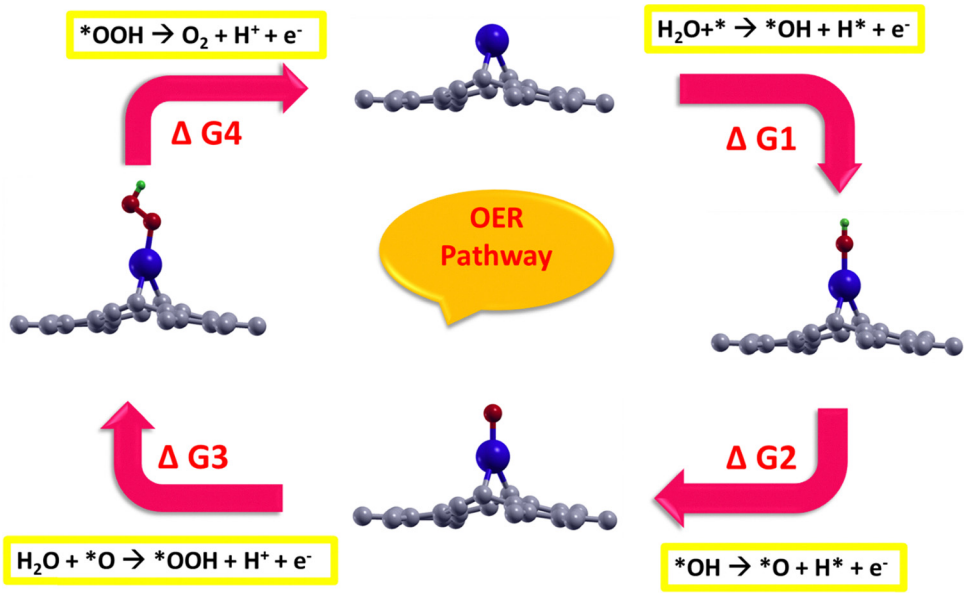

Fig. 5 Representation of the 4e⁻ OER process of the 4H site over TM-HGY with the optimized configurations for O, OH, and OOH (intermediates). Colour scheme: silver C; navy blue TM (TM = Au, Pt, Co, Cr, and Sc); red O; green H.

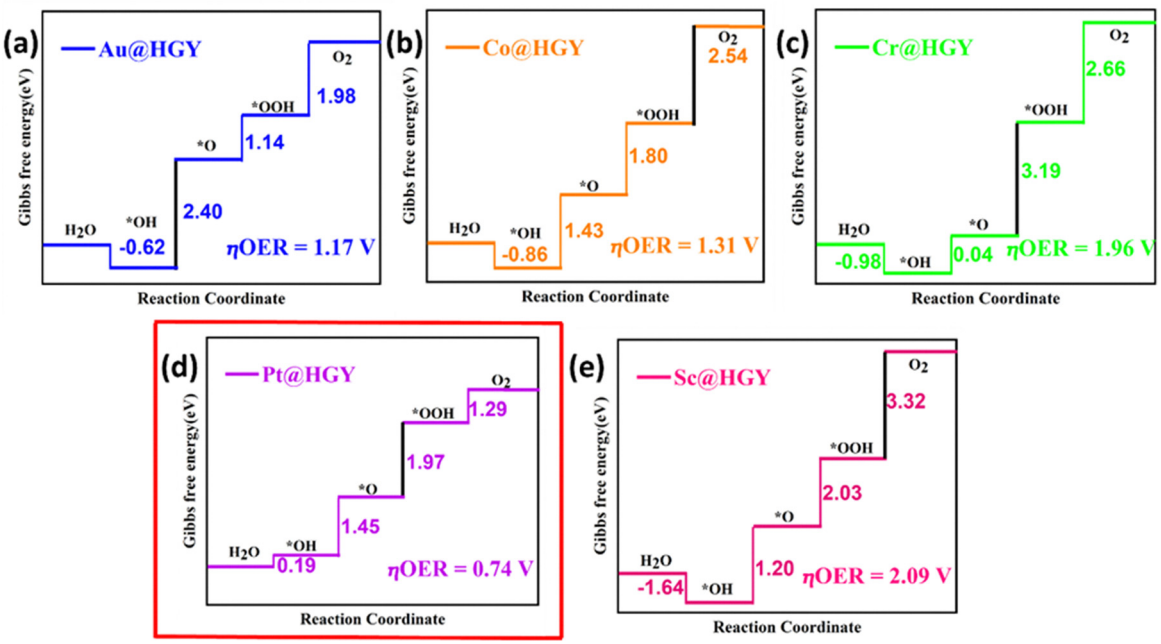

Fig. 6 Gibbs free energy diagram of the OER for (a) Au, (b) Co, (c) Cr, (d) Pt, and (e) Sc in HGY at zero potential.

bearing on the OER of the Pt@HGY system. The electronic properties of O, H, C, and Pt atoms are compared, and it is found that O exhibits the optimum electronegativity. Additionally, the *O and *OOH formation phases were chosen because the incarnation of *O or *OOH was the crucial step in pursuing the redistribution of charge, and comprehending that the d block of the Pt atoms that exist in Pt@HGY for the OER mechanism are extensive *versus* a single atom of O as well as H. In all phases comprising the intermediates, Fig. 7 shows that the interaction between Pt and C is almost the same. It is found that the interaction betwixt O and Pt is negligible for both *O and *OOH when the Löwdin charge for transition state 3 amid the *O and *OOH is critiquing. Fig. 7(f) makes it clear that when OOH is attached, the charges of oxygen atoms only slightly change, yet the charges of H atoms drop relative to OH [Fig. 7e]. Table S2, where the bond length represents the electron cloud of the two elements, offers an additional comprehension method. According to Table S2, Pt@HGY + OH has

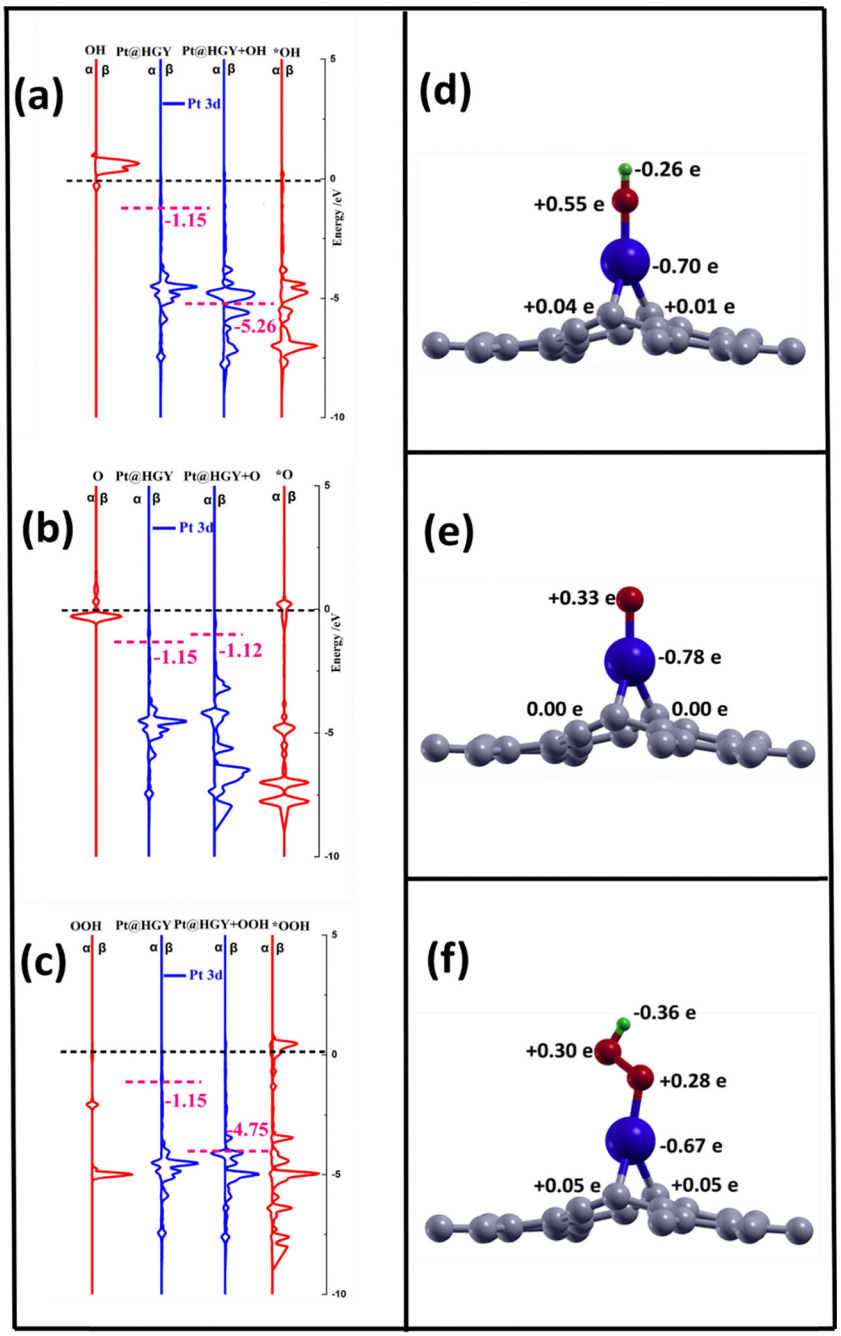

Fig. 7 (a)–(c) PDOS and diagrammatic representation of 3d orbitals of Pt@HGY, where the solid blue line embodies the Pt 3d orbitals. 2p orbitals of intermediates prior and subsequent to the adsorption on the Pt@HGY substrate. The pink dotted line marks the position of the d band centre of the Pt@HGY substrate prior and subsequent to the adsorption of O, OH, and OOH. Löwdin charge analysis (d)–(f) of the corresponding adsorbed OH, O, and OOH. Colour scheme: silver C; navy blue Pt; green H; red O.

a bond length of 1.82 Å between Pt and O. Likewise, Pt@HGY + OOH has a total bond length of 4.4 Å, with the bond lengths among Pt–O, O–O, along with O–H being 1.98, 1.45, and 0.97 angstrom. An increase in bond length, which results in a decreased occurrence of charge transfer, is responsible for the H atom's charge decreasing from −0.26 to −0.36*e*. It is clear that the total charges show an upward trend in transition state III, which is betwixt the *O and *OOH functional groups. This observation suggests that the overall direction of electron transmission during the hydroxyl adsorption process is from the bottom to the top. A new charge equilibrium is ultimately established by the structure following the adsorption process.

The significance of the d-band centre as a crucial electronic structural descriptor controlling the OER catalytic activity has been demonstrated by a number of earlier investigations. In order to facilitate charge transfer and catalytic performance, Guoyu *et al.* reported that the FeCu/NC catalyst has an optimally positioned d-band centre at about −1.806 eV, which

correlates with its low OER overpotential and enhanced density of states (DOS) near the Fermi level.[48] Similar to this, Sun *et al.* showed that the OER overpotential of Ir@NiN_2 (0.28 V) is linearly related to the location of the metal d-band centre, indicating its crucial function in regulating the catalytic efficiency and adsorption strength.[51]

Volcano plot and scaling relationship of pristine HGY and TM@HGY

The overpotential and the strength of the interaction between intermediates and active atoms are typically characterized in the OER process by examining the relationship among the Gibbs free energy of three intermediates (ΔG^*_{OH}, ΔG^*_O, and ΔG^*_{OOH}). The scaling relationship between the ΔG^*_{OH} and $\Delta G^*_{OOH}$of the analyzed HGY and TM-doped HGY are shown in Fig. 8(a). Among the four elementary stages, the deprotonation process $\left(\Delta G^*_O - \Delta G^*_{OH}\right)$, or the creation of OOH species $\left(\Delta G^*_{OOH} - \Delta G^*_O\right)$ typically exhibits the highest free energy shift, serving as the PDS. Additionally, the difference between ΔG^*_O and ΔG^*_{OOH} can be employed as a descriptor of overpotential (η) in the volcanic map based on the scaling relationship betwixt ΔG^*_{OH} and ΔG^*_{OOH} $\left(\Delta G^*_{OH} = \Delta G^*_{OOH} + 3.2\ \text{eV}\right)$. The scaling relation, where $\Delta G^*_{OH} = 0.80\Delta G^*_{OOH} + 3.64$ eV, is usually met, as Fig. 8(a) illustrates. A good match is demonstrated by the intercept and slope, which have modest deviations within a respectable range ($R^2 = 0.85$).

The overpotential η_{OER} can be computed by comparing the potentials of ΔG^*_{OOH} and ΔG^*_O, as the potential determining stages of the OER for both pristine as well as TM-doped HGY predominantly occur during the $\Delta G3$ (OOH* to O*) transition. The η_{OER} was characterized using the $\Delta G^*_{OOH} - \Delta G^*_O$ descriptor, and a graph of the volcano curve can be produced (refer to Fig. 8(b)). The matching overpotentials for every type are additionally presented in the volcano plot for easy viewing. Therefore, the discovery of the Pt top in HGY at the volcano's summit attests to the system's better electrocatalytic activities relative to other pristine sites and TM-anchored HGY.

Structural along with thermal stability by MD simulations of Pt@HGY

DFT simulations are conducted at 0 K, which may not be indicative of the structure at ambient temperature or at higher temperatures. Specifically, in the case of the OER, the substrate needs to maintain its structural integrity both at normal temperatures, then during the process of desorption, ensuring that the substrate may be used again in the subsequent cycle. At the outset, the temperature of Pt@HGY was increased to 500 K in a microcanonical way in a duration of 5 ps with 1 fs time step. During the subsequent phase, the system was brought to a state of equilibrium at a temperature of 500 K by applying heat through a Nose–Hoover thermostat in a canonical way. This process was carried out using the VASP code.

Using MD simulations at an equilibrium temperature of 500 K, the bond length variation of C–C (1.32 Å) and Pt–C (1.98 Å) atomic pairs has been shown over a period of 3500 fs (Fig. 9(a)). According to the research, these atomic pairs obligated a net bond length fluctuation of 1.18% and 2.59%. The slight variation seen could be attributed to the thermal excitations causing the mobility of the Pt atom. Considering the thermal vibrations of the Pt atom, the higher temperature does not have a notable impact on the stability of the adorned structure. Therefore, the doping of Pt on the HGY system is likely to remain very stable even at elevated temperatures, which makes the system well-suited for adsorbing intermediates intricate in the OER mechanism. Fig. 9(b) displays the variations in temperature and total energy as a function of the simulated time steps. No signs of deterioration were observed in the Pt@HGY framework, confirming the thermodynamic stability of the structure at high temperatures.

A comprehensive comparison between the present work, HGY and TM-anchored HGY, and previously reported nanomaterials is presented in Table 1. Based on the results presented in Fig. 5, it can be concluded that Pt's OER activity in HGY surpasses that of both pristine and other doped TMs, such as Au, Co, Cr, and Sc.

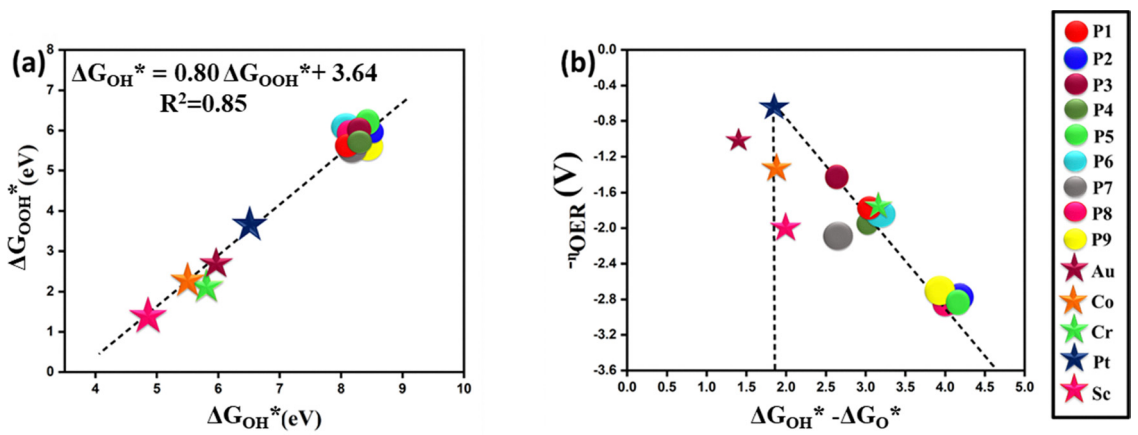

Fig. 8 (a) Scaling relations between ΔG^*_{OH} and ΔG^*_{OOH}; (b) volcano curve between negative OER overpotential ($-\eta_{OER}$) and $\Delta G^*_{OOH} - \Delta G^*_O$ for HGY and TM@HGY.

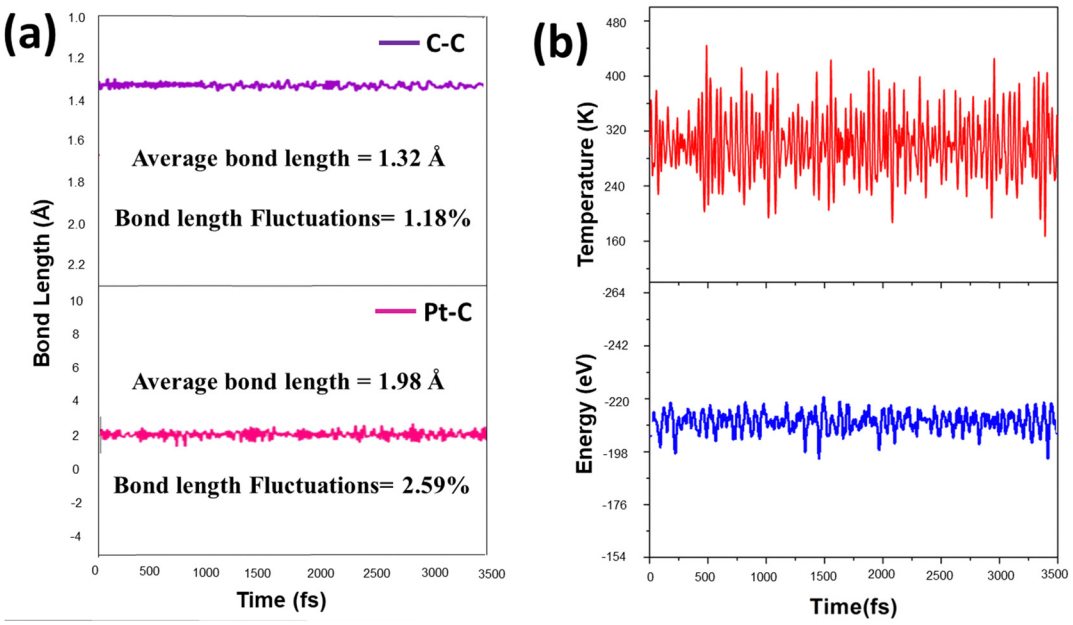

Fig. 9 (a) Bond length fluctuation of Pt–C and C–C atomic pairs of Pt@HGY at 500 K and (b) temperature along with total energy fluctuation with respect to the MD simulation step at 500 K for Pt@HGY.

Table 1 The computed η of TM@HGY is compared to previously published nanomaterials, respectively

System	η (V)	Ref.
Co@GY	0.77	52
Ni@3B-GY	0.53	52
graN-γ-GY@Rh	0.27	53
Co@R graphyne	0.74	54
Ni@R graphyne	0.31	54
Ni@H4,4,4-GY	0.34	55
Co@GY/Mn@GY	Co = 0.92 Mn = 2.96	56
Co@GY/Fe@GY	Co = 0.98 Fe = 1.62	56
Co@GY/Ni@GY	Co = 0.38 Ni = 0.86	56
Co@GY/Cu@GY	Co = 0.78 Cu = 1.21	56
Co@GY/Co@GY	0.55	56
Co@GY/GY	0.53	56
Ni@S-GPY	0.43	57
Pt@S-GPY	0.59	57
Ir@S-GPY	0.36	57
Pd@S-GPY	0.40	57
HGY	1.41	Present work
Pt@HGY	0.74	Present work

Conclusions

The electronic structural properties of HGY and TM-doped HGY, as well as their respective OER performance, are analysed using DFT. The catalytic reaction mechanism is then analysed in detail for Pt@HGY, which exhibits the greatest catalytic performance. The findings indicate a strong correlation betwixt the adsorption characteristics of the material and the position of the d band centre. The analysis of the overpotential along with d band centre illustration reveals that the activation energy barrier of the OER can be diminished by modulating the d band centre in a direction that deviates from the Fermi level. The suitability of the d band centre position at −1.15 eV for achieving a balance between dissociation as well as adsorption of OER intermediates has been demonstrated. The partial density of states and Löwdin charge transfer findings indicate that the presence of unoccupied antibonding orbitals in Pt@HGY facilitates the adsorption process with the intermediate, leading to surface delocalization. Additionally, the interaction between the metal d orbital with the middle sp orbital leads to a reduction of the d band centre and a favourable range for bond length adsorption. Moreover, it has been observed that the Pt element continues to be attached to HGY even when exposed to elevated temperatures of up to 500 K. The aforementioned outcome confirms the structure's thermal stability, which is supported by *ab initio* MD simulations. This study offers valuable insights into the catalytic performance of Pt-anchored HGY for the oxygen evolution reaction, as well as the design strategy for generating high OER activity in transition metal-anchored holey graphyne.

Conflicts of interest

There are no conflicts to declare.

Data availability

All data supporting this study are included within the article and the SI, and are available from the corresponding author upon reasonable request. The authors will make the data publicly available in an appropriate repository upon publication. Supplementary information is available. See DOI: **https://doi.org/10.1039/d5cp02097b.**

Acknowledgements

KSJ expresses profound gratitude to the University Grants Commission (UGC) for administering the Savitribai Jyotirao Phule Fellowship for Single Girl Child (SJSGC). The authors highly acknowledge Charotar University of Science and Technology for providing computational facilities (PARAM Shavak and VISHNU cluster). The authors acknowledge BARC's Supercomputing facility where part of the simulations were carried out.

References

1 G. Yasin, S. Ibraheem, S. Ali, M. Arif, S. Ibrahim, R. Iqbal, A. Kumar, M. Tabish, M. A. Mushtaq, A. Saad, H. Xu and W. Zhao, Defects-engineered tailoring of tri-doped interlinked metal-free bifunctional catalyst with lower Gibbs free energy of OER/HER intermediates for overall water splitting, *Mater. Today Chem.*, 2022, **23**, 100634, DOI: **10.1016/J.MTCHEM.2021.100634**.

2 X. Gong, J. Ge, J. Qi, H. Ding, L. Zhang, P. Ma, Z. Chen, N. Zhang, J. Xu, L. Zhu, J. Lu, G. Li, J. Ge and Y. Ye, Copper-doped nickel–iron metal/metal oxide electrode with improved performance by promoting synergistic effects in the oxygen evolution reaction, *Mater. Today Chem.*, 2024, **40**, 102225, DOI: **10.1016/J.MTCHEM.2024.102225**.

3 S. Song, Y. Fu, F. Yin, Y. Zhang, J. Ma, Y. Liu, J. Ren, W. Ye and R. Ma, NiFe-based tungstate@layered double hydroxide heterostructure supported on graphene as efficient oxygen evolution reaction catalyst, *Mater. Today Chem.*, 2023, **28**, 101369, DOI: **10.1016/J.MTCHEM.2022.101369**.

4 Z. A. Sheikh, D. Vikraman, H. Kim, S. Aftab, S. F. Shaikh, F. Shahzad, J. Jung, H. S. Kim, S. Hussain and D. K. Kim, Perovskite oxide-based nanoparticles embedded MXene composites for supercapacitors and oxygen evolution reactions, *J. Energy Storage*, 2024, **81**, 110342, DOI: **10.1016/J.EST.2023.110342**.

5 P. Li, H. Yang and Q. Wang, Enhanced oxygen evolution reaction and lithium-ion storage performance of MOF-derived $NiCo_2O_4$-NiO-Co@graphene composites: Effect of carboxylic ligand group, *J. Energy Storage*, 2024, **84**, 110823, DOI: **10.1016/J.EST.2024.110823**.

6 R. Saini, F. Naaz, A. H. Bashal, A. H. Pandit and U. Farooq, Recent advances in nitrogen-doped graphene-based heterostructures and composites: mechanism and active sites for electrochemical ORR and HER, *Green Chem.*, 2024, **26**, 57–102, DOI: **10.1039/D3GC03576J**.

7 W. Li, M. Sohail, U. Anwar, T. A. Taha, A. G. Al-Sehemi, S. Muhammad, A. A. Al-Ghamdi, M. A. Amin, A. Palamanit, S. Ullah, A. Hayat and Z. Ajmal, Recent progress in g–C_3N_4–Based materials for remarkable photocatalytic sustainable energy, *Int. J. Hydrogen Energy*, 2022, **47**, 21067–21118, DOI: **10.1016/J.IJHYDENE.2022.04.247**.

8 A. Hayat, M. Sohail, J. Ali Shah Syed, A. G. Al-Sehemi, M. H. Mohammed, A. A. Al-Ghamdi, T. A. Taha, H. Salem AlSalem, A. M. Alenad, M. A. Amin, A. Palamanit, C. Liu, W. I. Nawawi, M. Tariq Saeed Chani and M. Muzibur Rahman, Recent Advancement of the Current Aspects of g-C_3N_4 for its Photocatalytic Applications in Sustainable Energy System, *Chem. Rec.*, 2022, **22**, DOI: **10.1002/TCR.202100310**.

9 A. Curutchet, P. Colinet, C. Michel, S. N. Steinmann and T. Le Bahers, Two-sites are better than one: Revisiting the OER mechanism on CoOOH by DFT with electrode polarization, *Phys. Chem. Chem. Phys.*, 2020, **22**, 7031–7038, DOI: **10.1039/d0cp00281j**.

10 A. Curutchet, P. Colinet, C. Michel, S. N. Steinmann and T. Le Bahers, Two-sites are better than one: revisiting the OER mechanism on CoOOH by DFT with electrode polarization, *Phys. Chem. Chem. Phys.*, 2020, **22**, 7031–7038, DOI: **10.1039/D0CP00281J**.

11 Y. Li, Z. Zhu, Y. L. Zhong, Y. Jin, P. Saha and Q. Cheng, Heterogeneous Cr-doped Co_3S_4/$NiMoS_4$ bifunctional electrocatalyst for efficient overall water splitting, *J. Power Sources*, 2024, **614**, 234969, DOI: **10.1016/J.JPOWSOUR.2024.234969**.

12 A. Mahmood, G. Lu, X. Wang, Y. Wang, X. Xie and J. Sun, Investigating the stability and role of defects in vertically aligned WS2/MoS2 heterojunctions on OER activity using first principles study, *J. Power Sources*, 2022, **551**, 232208, DOI: **10.1016/J.JPOWSOUR.2022.232208**.

13 M. I. Jamesh and X. Sun, Recent progress on earth abundant electrocatalysts for oxygen evolution reaction (OER) in alkaline medium to achieve efficient water splitting – A review, *J. Power Sources*, 2018, **400**, 31–68, DOI: **10.1016/J.JPOWSOUR.2018.07.125**.

14 H. Wang, Y. Yuan, J. Gu, Z. Jia, Z. Lu, Z. Bai, L. Yang and X. Yang, Facile one-pot synthesis of layered double hydroxides nanosheets with oxygen vacancies grown on carbon nanotubes for efficient oxygen evolution reaction, *J. Power Sources*, 2020, **467**, 228354, DOI: **10.1016/J.JPOWSOUR.2020.228354**.

15 J. Chen, C. Cai, Y. Sun, B. Sun, H. Wang, Y. Tang and Y. Chen, Hierarchical-hollow architecture NiSe2 nanosheets for overall water splitting, *Electrochim. Acta*, 2024, **493**, 144443, DOI: **10.1016/J.ELECTACTA.2024.144443**.

16 X. Chen, H. Zhu, J. Zhu and H. Zhang, Indium-based bimetallic clusters anchored onto silicon-doped graphene as efficient multifunctional electrocatalysts for ORR, OER, and HER, *Chem. Eng. J.*, 2023, **451**, 138998, DOI: **10.1016/J.CEJ.2022.138998**.

17 L. Jin, C. Liu, D. Wang, M. Liu, T. G. Lee, S. G. Peera and X. Qi, CdN_4C_0-gra as efficient trifunctional electrocatalyst for the HER, OER and ORR: A density functional theory study, *Appl. Surf. Sci.*, 2023, **610**, 155580, DOI: **10.1016/J.APSUSC.2022.155580**.

18 R. V. Mom, J. Cheng, M. T. M. Koper and M. Sprik, Modeling the Oxygen Evolution Reaction on Metal Oxides: The Influence of Unrestricted DFT Calculations, *J. Phys. Chem. C*, 2014, **118**, 4095–4102, DOI: **10.1021/jp409373c**.

19 N. Abidi, A. Bonduelle-Skrzypczak and S. N. Steinmann, How to dope the basal plane of 2H-MoS_2 to boost the hydrogen evolution reaction?, *Electrochim. Acta*, 2023, **439**, 141653, DOI: **10.1016/J.ELECTACTA.2022.141653**.

20 Z. Yang, Y. Chen, Y. Chang, X. Song, J. Wang and H. Li, Synergetic effect of both cation and anion doping cobalt

oxides on V2C MXene boosting oxygen evolution reaction, *J. Power Sources*, 2024, **604**, 234422, DOI: 10.1016/J.JPOWSOUR.2024.234422.

21 H. Xu, J. Li and X. Chu, Intensifying Hydrogen Spillover for Boosting Electrocatalytic Hydrogen Evolution Reaction, *Chem. Rec.*, 2023, **23**, e202200244, DOI: 10.1002/TCR.202200244.

22 K. A. Baseden and J. W. Tye, Introduction to density functional theory: Calculations by hand on the helium atom, *J. Chem. Educ.*, 2014, **91**, 2116–2123, DOI: 10.1021/ED5004788/ASSET/IMAGES/MEDIUM/ED-2014-004788_0003.GIF.

23 Y. Yu, J. Zhou and Z. Sun, Novel 2D Transition-Metal Carbides: Ultrahigh Performance Electrocatalysts for Overall Water Splitting and Oxygen Reduction, *Adv. Funct. Mater.*, 2020, **30**, 2000570, DOI: 10.1002/ADFM.202000570.

24 P. Rani, G. S. Dubey and V. K. Jindal, DFT study of optical properties of pure and doped graphene, *Phys. E*, 2014, **62**, 28–35, DOI: 10.1016/J.PHYSE.2014.04.010.

25 M. Alsagri, A. Laref, B. Ul Haq, H. R. AlQahtani, F. T. Nya, M. El Amine Monir, S. Chowdhury, E. A. Alghamdi, H. M. Huang, J. T. Yang and Y. C. Xiong, The effect of non-metals (O, F) dopant on the electronic structure, Dirac cone, and optical characteristics of graphene sheets applicable for gas sensing, *J. Mol. Struct.*, 2024, **1299**, 137102, DOI: 10.1016/j.molstruc.2023.137102.

26 S. Gupta, P. Pimenidou, M. Garcia, S. Das and N. Dimakis, First-principles calculations integrated with experimental optical and electronic properties for MoS2-graphene heterostructures and MoS2-graphene-Au heterointerfaces, *Appl. Surf. Sci.*, 2023, **623**, 156948, DOI: 10.1016/j.apsusc.2023.156948.

27 M. Houmad, H. Zaari, A. Benyoussef, A. El Kenz and H. Ez-Zahraouy, Optical conductivity enhancement and band gap opening with silicon doped graphene, *Carbon*, 2015, **94**, 1021–1027, DOI: 10.1016/j.carbon.2015.07.033.

28 Z. G. Shao and Z. L. Sun, Optical properties of α-, β-, γ-, and 6,6,12-graphyne structures: First-principle calculations, *Phys. E*, 2015, **74**, 438–442, DOI: 10.1016/J.PHYSE.2015.07.011.

29 C. C. Zhao, S. H. Tan, Y. H. Zhou, R. J. Wang, X. J. Wang and K. Q. Chen, Half-metallicity and high spin-filtering effect of magnetic atoms embedded zigzag 6,6,12-graphyne nanoribbon, *Carbon*, 2017, **113**, 170–175, DOI: 10.1016/j.carbon.2016.11.022.

30 P. Lazić and Z. Crljen, Graphyne on metallic surfaces: A density functional theory study, *Phys. Rev. B: Condens. Matter Mater. Phys.*, 2015, **91**, 125423, DOI: 10.1103/PHYSREVB.91.125423.

31 D. Chodvadiya, B. Chakraborty and P. K. Jha, Transition metal atoms anchored 2D holey graphyne for hydrogen evolution reaction: Acumen from DFT simulation, *Int. J. Hydrogen Energy*, 2023, **48**, 18326–18337, DOI: 10.1016/J.IJHYDENE.2023.01.246.

32 X. Liu1, S. M. Cho, S. Lin, E. Yun, E. H. Baek, Z. Chen, D. H. Ryu and H. Lee, Direct Band Gap Semiconducting Holey Graphyne: Structure, Synthesis and Potential Applications, *arXiv*, 2019, preprint, arXiv:1907.03534v1, DOI: 10.48550/arXiv.1907.03534v1, https://arxiv.org/abs/1907.03534v1 (accessed March 7, 2024).

33 Y. Gao, H. Zhang, H. Pan, Q. Li and J. Zhao, Ultrahigh hydrogen storage capacity of holey graphyne, *Nanotechnology*, 2021, **32**, 215402, DOI: 10.1088/1361-6528/abe48d.

34 X. Liu, S. Min Cho, S. Lin, Z. Chen, W. Choi, Y.-M. Kim, E. Yun, E. Hee Baek, D. Hyun Ryu and H. Lee, Constructing two-dimensional holey graphyne with unusual annulative π-extension, *Matter.*, 2022, **5**, 2306–2318, DOI: 10.1016/j.matt.2022.04.033.

35 J. Dewangan, V. Mahamiya, A. Shukla and B. Chakraborty, Reversible hydrogen adsorption in Ti-functionalized porous holey graphyne: Insights from first-principles calculation, *Energy Storage*, 2022, **5**, e391, DOI: 10.1002/EST2.391.

36 M. Singh, A. Shukla and B. Chakraborty, An *Ab initio* study of the y decorated 2D holey graphyne for hydrogen storage application, *Nanotechnology*, 2022, **33**, 405406, DOI: 10.1088/1361-6528/ac7cf6.

37 S. Lakshmy, A. Kundu, N. Kalarikkal and B. Chakraborty, Pristine and transition metal decorated holey graphyne monolayer as an ammonia sensor: insights from DFT simulations, *J. Phys. D: Appl. Phys.*, 2023, **56**, 055402, DOI: 10.1088/1361-6463/ACAE2E.

38 M. Ren, X. Guo, S. Zhang, S. Huang, M. Ren, S. Huang, X. Guo and S. Zhang, Design of Graphdiyne and Holey Graphyne-Based Single Atom Catalysts for CO2 Reduction With Interpretable Machine Learning, *Adv. Funct. Mater.*, 2023, **33**, 2213543, DOI: 10.1002/ADFM.202213543.

39 M. Sajjad, K. Badawy, J. A. Larsson, R. Umer and N. Singh, Two dimensional holey graphyne: An excellent anode and anchoring material for metal–ion and metal–sulfur batteries, *Carbon*, 2023, **214**, 118340, DOI: 10.1016/J.CARBON.2023.118340.

40 B. Mortazavi, Electronic, Thermal and Mechanical Properties of Carbon and Boron Nitride Holey Graphyne Monolayers, *Materials*, 2023, **16**, 6642, DOI: 10.3390/MA16206642.

41 Y.-C. Jiang, T. Kariyado and X. Hu, Topological electronic states in holey graphyne, *Nanotechnology*, 2023, **35**, 195201, DOI: 10.1088/1361-6528/ad2483.

42 N. Argaman and G. Makov, Density Functional Theory – an introduction, *Am. J. Phys.*, 2000, **68**, 69–79, DOI: 10.1119/1.19375.

43 P. Giannozzi, O. Baseggio, P. Bonfà, D. Brunato, R. Car, I. Carnimeo, C. Cavazzoni, S. De Gironcoli, P. Delugas, F. Ferrari Ruffino, A. Ferretti, N. Marzari, I. Timrov, A. Urru and S. Baroni, Quantum ESPRESSO toward the exascale, *J. Chem. Phys.*, 2020, **152**, 154105, DOI: 10.1063/5.0005082.

44 J. P. Perdew and K. Burke, Generalized gradient approximation for the exchange-correlation hole of a many-electron system, *Phys. Rev. B.: Condens. Matter. Mater. Phys.*, 1996, **54**, 16533–16539, DOI: 10.1103/PHYSREVB.54.16533.

45 S. Grimme, Semiempirical GGA-type density functional constructed with a long-range dispersion correction, *J. Comput. Chem.*, 2006, **27**, 1787–1799, DOI: 10.1002/jcc.20495.

46 J. Hafner, *Ab initio* simulations of materials using VASP: Density-functional theory and beyond, *J. Comput. Chem.*, 2008, **29**, 2044–2078, DOI: 10.1002/JCC.21057.

47 X. Li, Z. Cheng and X. Wang, Understanding the Mechanism of the Oxygen Evolution Reaction with Consideration of Spin, Electrochem, *Energy Rev.*, 2021, **4**, 136–145, DOI: 10.1007/S41918-020-00084-1/METRICS.

48 G. Hou, Y. Song, X. Ma, F. Chu, M. Wu, D. Wang, J. Wu, Y. Qi, C. Wu and M. Xiong, First principles study on electronic properties and oxygen evolution mechanism of 2D bimetallic N-doped graphene, *J. Mol. Graphics Modell.*, 2022, **111**, 108101, DOI: 10.1016/J.JMGM.2021.108101.

49 S. Lakshmy, A. Kundu, N. Kalarikkal and B. Chakraborty, Catechol sensor based on pristine and transition metal embedded holey graphyne: a first-principles density functional theory study, *J. Mater. Chem. B*, 2022, **10**, 5958–5967, DOI: 10.1039/D2TB00754A.

50 Y. Wang, W. Tian, J. Wan, W. Fu, H. Zhang, Y. Li and Y. Wang, Probing the origin of group VB transition metal monocarbides for high-efficiency hydrogen evolution reaction: A DFT study, *Appl. Surf. Sci.*, 2021, **539**, 148312, DOI: 10.1016/J.APSUSC.2020.148312.

51 D. Y. Sun, L. H. Li, G. T. Yuan, Y. Lou Ouyang, R. Tan, W. J. Yin, X. L. Wei and Z. K. Tang, Enhanced OER catalytic activity of single metal atoms supported by the pentagonal NiN2 monolayer: insight from density functional theory calculations, *Phys. Chem. Chem. Phys.*, 2024, **26**, 6292–6299, DOI: 10.1039/D3CP05464K.

52 M. Guo, M. Ji and W. Cui, Theoretical investigation of HER/OER/ORR catalytic activity of single atom-decorated graphyne by DFT and comparative DOS analyses, *Appl. Surf. Sci.*, 2022, **592**, 153237, DOI: 10.1016/J.APSUSC.2022.153237.

53 Y. Qin, M. Yang, C. Deng, W. Shen, R. He and M. Li, Theoretical insight into single Rh atoms anchored on N-doped γ-graphyne as an excellent bifunctional electrocatalyst for the OER and ORR: electronic regulation of graphitic nitrogen, *Nanoscale*, 2021, **13**, 5800–5808, DOI: 10.1039/D0NR07513B.

54 C. Li, T. Li, G. Yu and W. Chen, Theoretical Investigation of HER and OER Electrocatalysts Based on the 2D R-graphyne Completely Composed of Anti-Aromatic Carbon Rings, *Molecules*, 2023, **28**, 3888, DOI: 10.3390/MOLECULES28093888/S1.

55 H. Zhang, W. Wei, S. Wang, H. Wang, B. Huang and Y. Dai, H4,4,4-graphyne with double Dirac points as high-efficiency bifunctional electrocatalysts for water splitting, *J. Mater. Chem. A*, 2021, **9**, 4082–4090, DOI: 10.1039/D0TA10767K.

56 X. Gao, L. Mei, Y. Zhou and Z. Shen, Impact of electron transfer of atomic metals on adjacent graphyne layers on electrochemical water splitting, *Nanoscale*, 2020, **12**, 7814–7821, DOI: 10.1039/C9NR10579D.

57 X. Liu, G. Li, J. Liu and J. Zhao, Transition metal atoms anchored on square graphyne as multifunctional electrocatalysts: A computational investigation, *Mol. Catal.*, 2022, **531**, 112706, DOI: 10.1016/J.MCAT.2022.112706.